DESIGN STUDY OF A TWO-PANEL HEAD-AND-NECK CANCER DEDICATED POSITRON EMISSION TOMOGRAPHY SYSTEM

BY

MOHAN LI

THESIS

Submitted in partial fulfillment of the requirements for the degree of
Master of Science in Nuclear, Plasma, and Radiological Engineering
in the Graduate College of the
University of Illinois at Urbana-Champaign, 2018

Urbana, Illinois

Masters Committee:

Assistant Professor Shiva Abbaszadeh
Professor Rizwan Uddin

Abstract

Head and neck cancer (HNC) is collectively a group of cancers that usually begin in mucosal surfaces inside the head and neck. Due to the complex anatomy and vital physiological role of the tumor-involved regions, the goal of HNC treatment is not only to improve survival outcomes but also to preserve organ function. Whole-body (WB) positron emission tomography (PET) has been widely used for HNC diagnosis and treatment, but its low spatial resolution limits the management of HNC. A higher spatial resolution and a better contrast image will allow radiation oncologists to accurately measure the boundaries of tumors, design the planned target volume dose, and thus offer more freedom to choose treatment options such as surgery, radiation therapy, chemotherapy and targeted therapy.

To achieve a better management of HNC, this dissertation proposes a HNC dedicated PET system, which is supposed to replace the dedicated protocol in hospitals. The performance of a proposed system is studied using a Monte Carlo simulation. The noise equivalent count rate of the dedicated system is 9.3 $kcps$ at 5.7 kBq/cm^3, and it increases to 10.5 $kcps$ at 5.7 kBq/cm^3 with a lead shielding. The photon sensitivity is 0.83% for a point source placed at the field of view (FOV) centre. With a 2 mm full width at half maximum (FWHM) depth of interaction resolution, the system achieves 1 mm orthogonal-panel and 1.5 mm parallel-panel spatial resolution, and a 2 mm diameter hot rod is visible. Multiple scattering events are recovered and the entire FOV has a relatively uniform improvement of sensitivity. Signal-to-noise ratio and contrast-to-noise ratio of the reconstructed image improve 41.4% and 29.2% respectively after incorporating recovered multiple scattering events. Compared with a commercial WB PET system (GE Discovery MI), the proposed dedicated system shows an 830% improvement of noise equivalent count rate, a 36.1% improvement of photon coincidence sensitivity and a better spatial resolution and lesion visualization capability. Further

hardware-level work such as detector module design and characterization are on-going to validate these initial results.

To my parents, for their love and support.

Acknowledgments

It is a tremendous experience for me to perform the research work at the Radiological Instrumentation Laboratory (RIL).

First of all, I would like to express my deep gratitude and appreciation to my advisor Prof. Shiva Abbaszadeh, who has been a great teacher, mentor as well as the most trustworthy source of guidance and support through this project. I have learnt immensely from her vast experience in detector instrumentation, meticulous attitude towards working and the collaborative culture she nurtures at RIL.

I would also like to thank the member of my dissertation reading committee, Prof. Rizwan Uddin, for your support and informative suggestions.

This work gets generous help and support of my colleagues Zheng Liu and Sheng Yang at RIL. I learnt a lot from many inspiring conversations with them.

I would like to thank the Molecular Imaging Instrumentation Laboratory at Stanford University for the help with the gpurecon program.

I would like to acknowledge the funding support from the Carle Illinois Collaborative Research Seed Funding.

Lastly, I would like express my deep gratitude to my parents for their sacrifices to support me, the faith in my and the unconditional love.

Table of Contents

List of Tables

List of Figures

Chapter 1

Introduction

Head and neck cancer (HNC) is collectively a group of cancers that usually begins in mucosal surfaces inside the head and neck including mouth, nose, throat, larynx, sinuses, or salivary glands. Positron emission tomography (PET) is an *in vivo*, noninvasive medical imaging modality that enables the visualization of biological activity in living organisms. Whole-body (WB) PET has been widely used for HNC diagnosis and treatment because of its high sensitivity and specificity [1].

The spatial resolution of WB PET is typically 4 to 6 mm [2], which causes the detection of lesions less than 10 mm in diameter less accurately. However, more than 40% of cervical lymph node metastases have been found to be present in lymph nodes smaller than 10 mm [3]. The poor spatial resolution of WB PET may hamper the detection of small lesions, delineation of tumor boundaries and the calculation of target volume dose, which affects the management of HNC.

This thesis presents the design of a two-panel HNC dedicated PET system, whose performance is evaluated through a Monte Carlo simulation. The proposed system has several distinguishing features as follows. First, instead of the ring geometry commonly used in WB PET, the proposed system is made up of two panels, which can be put in close proximity to patients' neck to improve photon sensitivity. Second, small crystals are deployed, which will improve the spatial resolution. Third, depth-of-interaction (DOI) capability is applied to reduce the parallax error and mitigate the non-isotropic spatial resolution, both of which are caused by the non-rotating two-panel geometry. Forth, multiple scattering events are recovered to improve the photon sensitivity and reduce the scanning time. Compared with GE Discovery MI (3-ring configuration), a cutting-edge commercial WB PET system, the proposed system shows a superior performance in terms of noise equivalent count (NEC) rate, photon coincidence sensitivity, spatial resolution and lesion vi-

sualization.

In Chapter 2, the principle of PET, photon detection, and PET imaging metrics are presented. Chapter 3 provides the need and design of the HNC dedicated PET system, and Chapter 4 reports the performance. Conclusion comes in Chapter 5.

Chapter 2

Positron emission tomography

2.1 Principle of PET

PET is an *in vivo*, noninvasive medical imaging modality that visualizes physiological processes by observing the distribution and concentration of biologically active compounds that participate in specific physiological processes [4]. The biologically active compounds are called radiotracers because they are radioactive and contain positron-emitting atoms.

For example, fluorodeoxyglucose (FDG) is a biological analog of glucose, where one of the hydroxyl groups is replaced by a positron-emitting atom ^{18}F [5]. Fig. 2.1 shows the molecular structure of glucose and FDG. Once introduced into an organism via injection into the tail vein, FDG follows an analogous metabolic process of glucose. Because glucose is a key source of energy, the concentration distribution of glucose represents the rate of metabolism. As a result, a correspondence between the rate of metabolism internal to organisms and externally detectable positron radioactivity is established by ^{18}F atoms [6].

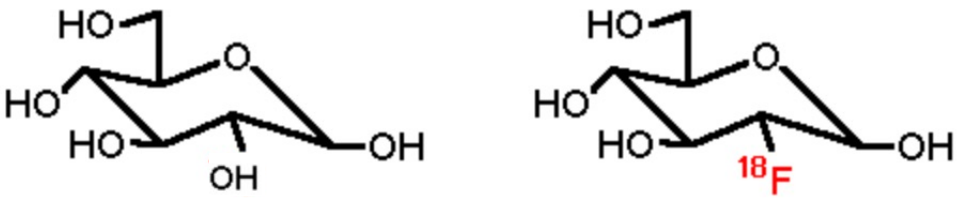

Figure 2.1: Left: molecular structure of glucose. Right: molecular structure of fluorodeoxyglucose.

About 96.7% of ^{18}F decay results in an emitted positron and a stable ^{18}O [7]. The emitted positron penetrates surrounding tissues, loses energy at the

same time, and eventually pairs up with an electron to form a positronium. The positronium is unstable and positron and electron annihilate each other very quickly, which results in the emission of a pair of photons. The momentum of positronium is almost zero. Due to the conservation of momentum, the pairs of photons are emitted approximately collinearly and anti-parallel to each other [8]. Due to the conservation of energy, the energy of each photon is equivalent to the mass of an electron or a positron, which is

$$\begin{aligned} E &= mc^2 \\ &= 9.109 \times 10^{-31}\ kg \times (2.998 \times 10^8\ m/s)^2 \\ &= 511.059\ keV, \end{aligned} \tag{2.1}$$

where E is the energy of one photon, m is the rest mass of an electron or positron and c is the speed of light in vacuum.

Annihilation photons are detected by surrounding photon detectors, which can register the spatial coordinates of the photon interaction. Once a pair of annihilation photons are detected, a line that joins the two photons interaction location can be drawn, which is called line of response (LOR) [9]. A positron-electron annihilation event must occur somewhere along a LOR, and thus a tomography image can be reconstructed based on LORs. Analytical image reconstruction algorithms such as direct Fourier reconstruction, filtered backprojection [10] and iterative image reconstruction algorithms such as maximum-likelihood estimation (MLEM) [11], and ordered subsets estimation (OSEM) [12], have been developed. Generally, analytical methods are fast and easy to implement, while iterative methods are more robust to noise. Interested readers can find more details in [13]. Fig. 2.2 shows the typical PET procedure.

2.2 Photon detection

The physics and techniques of photon detection for PET applications is described in this section.

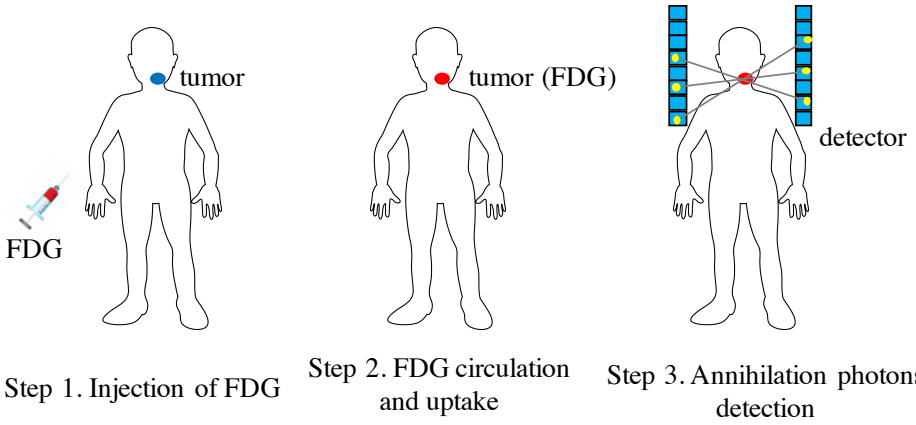

Figure 2.2: Typical PET scanning procedure.

2.2.1 Physics of photon detection

Photons are massless and chargeless elementary particles. Due to the electrical neutrality, photons do not lose energy continuously in medium through coulombic interactions like electrons. Instead, photons are stochastically scattered or absorbed when penetrating matters. The behavior can be described by Beer-Lambert Law [14], which is

$$I = I_0 e^{-\alpha d}, \tag{2.2}$$

where I_0 is the original photon flux, I is the photon flux without absorption or scattering at a depth d of a material and α is the linear attenuation coefficient of the material. Detecting material should have a large α so that it has a large photon interaction cross section. α accounts for contributions of different types of interactions. For 511 keV photons, the dominant interactions are the photoelectric effect and the Compton scattering [15].

In the photoelectric effect, the photon is absorbed by an inner shell electron, and the energy of the photon leads to the ejection of the electron from its atomic orbit. The electron is called a photoelectron, whose energy is given by

$$E_{pe} = E_p - E_b, \tag{2.3}$$

where E_{pe} and E_p are the energy of the photoelectron and the photon respectively and E_b is the orbital binding energy.

In the Compton scattering, the photon is scattered by an outer shell elec-

tron. As in the photoelectric effect, the electron is also ejected. However, the binding energy of an outer shell electron is small and can be ignored. Denote scattering angle as the deflection of the trajectory of the photon after interaction, the scattering angle has a one-to-one correspondence to the energy of scattered electron, which is given by

$$E_e = E_p - \frac{E_p}{2 - \cos\theta}, \tag{2.4}$$

where θ is the scattering angle, E_e is the energy of scattered electron and E_p is the energy of the photon before interaction, which is 511 keV [16]. In Compton scattering, $\theta \in (0,\ 180°]$. When θ is 0° (forward scattering), E_e is 0 keV. When θ is 180° (backward scattering), E_e is $2E_p/3$ keV.

The electron ejected through the photoelectric effect or the Compton scattering is called the primary charged particle. For a neutral particle like photon, primary charge particles must be produced before it can be detected.

2.2.2 Techniques of photon detection

Two common photon detection schemes are utilized for PET: 1). indirect detection using scintillators coupled to devices that converts visible lights to electrons; 2). direct detection using semiconductors.

Scintillator are transparent materials that exhibit the property of luminescence when excited by ionizing radiation. In PET imaging, both organic and inorganic scintillator materials are used. When the primary charged particle interacts with a scintillator, valence electrons are excited from the ground state (organic scintillators) or the valence band (inorganic scintillators). The excited valence electrons are called the secondary charged particle. Scintillation lights are emitted when the valence electrons de-excite. The measured photon energy is proportional to the number of scintillation lights. Commonly used scintillators in PET application include lutetium oxyorthosilicate (LSO), Lutetium-yttrium oxyorthosilicate (LYSO), gadolinium oxyorthosilicate (GSO), lanthanum(III) bromide ($LaBr_3$) and bismuth germanate (BGO). Table 2.1 compares the properties of the four scintillators [17].

The scintillation lights need to be further converted to electric signals. Commonly used conversion devices in PET includes photomultiplier tube

Table 2.1: Properties of different commonly used scintillators in PET [17].

Property	LSO	LYSO	GSO	$LaBr_3$	BGO
Light output [ph/MeV]	31000	32000	7600	65000	8500
Peak emission [nm]	420	420	420	360	480
Decay time [ns]	$40-47$	41	$30-60$	15	300
Refractive index	1.82	1.81	1.85	1.9	2.15
Density [g/cm^3]	7.4	7.1	6.71	5.29	7.13
Hygroscopic	no	no	no	yes	no

(PMT), avalanche photodiodes (APD) and silicon photomultiplier (SiPM). For PMT, electrons are generated when scintillation lights interacts with its photocathode, while for APD and SiPM, mobile electrons and holes are generated through the absorption of scintillation lights within the depletion region of a reverse-biased P-N junction. After the generation of charge carriers, all these devices utilize a bias to maintain and multiply the carrier drift and create the electric signal. Table 2.2 compares the properties of the three devices [18].

Table 2.2: Properties of PMT, APD and SiPM [18].

Property	PMT	APD	SiPM
Gain	10^6	50-1000	$\sim 10^6$
Rise time [ns]	~ 1	~ 5	~ 1
Quantum efficiency [%]	~ 25	~ 70	$\sim 25-75$
Bias [V]	> 1000	300-1000	30-80
Temperature sensitivity [%/°C]	< 1	~ 3	$1-8$
Magnetic field sensitivity	yes	no	no
Sensitive area	cm^2	mm^2	mm^2
Price/channel [$]	> 200	~ 100	~ 50

Semiconductors are materials with a intermediate band gap between conductors and insulators. When the primary charged particle penetrate through the semiconductor, it keeps loosing energy through Coulombic interactions and exciting valence electrons into the conduction band, creating both mobile electrons and holes. With a voltage bias, electrons drift to anodes while holes drift to cathodes, which induces charges on electrodes. The measured photon

energy is proportional to the cumulative charge induced on electrodes. Commonly used semiconductors include cadmium telluride (CdTe) and cadmium zinc telluride (CZT).

2.3 PET imaging metrics

To quantitatively describe a PET system or compare different PET systems, imaging metrics and terminology used in PET are introduced in this section. The metrics are chosen for their direct impact on the image quality, and are related to both the detector-level and system-level characteristics of a PET system.

2.3.1 Energy resolution

It is possible that annihilation photons scatter with the body of patient before they are detected by photon detectors. As shown in Fig. 2.3, in this case LOR no longer goes through the point where the annihilation photons are emitted, which results in an incorrect estimate of the radiotracer. If the two photons of a coincidence are from the same annihilation and neither of them scatters before getting detected, such a coincidence is called a true coincidence. As a comparison, if the photon pair are from the same annihilation, but either or both scatter before getting detected, it is called a scattering coincidence. Intuitively, scattering coincidences degrade the image accuracy.

An effective method to avoid recording scattering coincidences is to measure the energy of detected photons. Because photons lose energy in Compton scattering, an energy deposition which is less than 511 keV should indicate that the photon has scattering before get detected, and thus a coincidence made up by this photon should be discarded. This method is called energy gating, which requires photon detectors to measure photon energy precisely.

The precision of a photon detector measuring photon energy is quantitively defined as the energy resolution, which is generally defined as

$$Energy\ resolution = \frac{\Delta E}{E}, \tag{2.5}$$

where ΔE is the full width at half maximum (FWHM) fluctuation in mea-

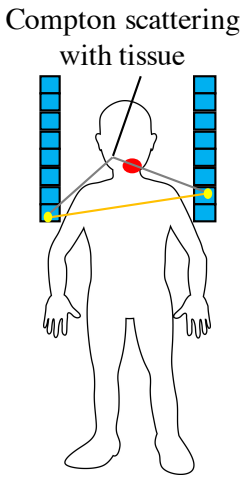

Figure 2.3: In a scattering coincidence event, annihilation photons scatter with tissue before getting detected. The grey lines show the real trajectory of photons, while the orange line is the measured LOR.

surement and E is the photon energy being measured, which is 511 keV in PET applications.

Except eliminating scattering coincidences, a good energy resolution is also beneficial to recover multiple scattering events. As in the soft tissue, photons can have both photoelectric effect and Compton scattering in detecting materials, and Compton interactions are often followed by subsequent Compton or photoelectric interactions, which is referred as multiple scattering events. As explain in [19], a photon detector that can accurately measure the position and energy deposition of individual photon interactions can effectively identify the first interaction in a multiple scattering event. As a result, a correct LOR can be formed and thus multiple scattering events can be used for image reconstruction.

2.3.2 Coincidence time resolution

Detected photons are paired with another photon that is close in time to form a LOR. The precision that a photon detector can measure the time difference of two annihilation photons is referred as the coincidence time resolution. To acquire the coincidence time resolution, a time window is set in advance and any pairs of photons detected within the duration of the time window are recorded. The FWHM of the time difference of the recorded coincidences is

used to represent the coincidence time resolution. This method is called time gating.

Due to the limited precision of time measurement, two photons from different annihilations may be paired up, which is called a random coincidence as shown in Fig. 2.4. To eliminate random coincidences, a small value of time window is desirable. However, a too small time window may also eliminate true coincidences. Generally, the time window is set as approximately twice as the coincidence time resolution.

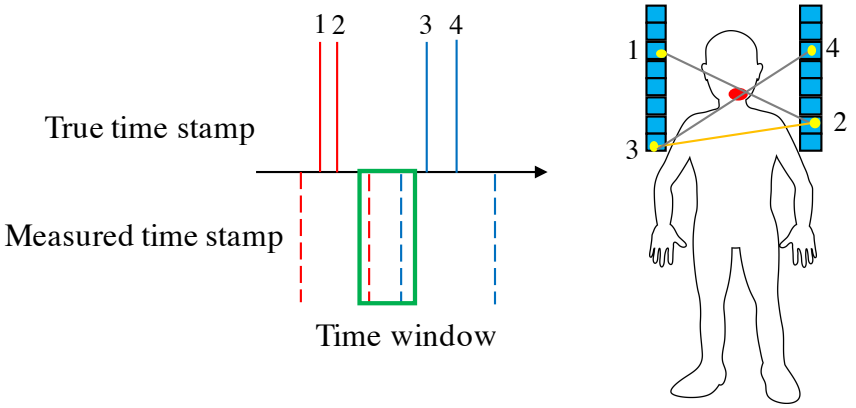

Figure 2.4: Explanation of the random coincidence due to limited precision of time measurement. Grey lines represents true coincidences, while the orange line corresponds to the random coincidence.

Except eliminating random coincidences, a good time resolution may also help to localize the position of annihilation. Fig. 2.5 shows an image enhancement technique called time of flight (TOF) imaging. Specifically, TOF detectors assign higher likelihood to a specific segment of a LOR, where the annihilation has a larger probability to happen. Interested readers can find more details in [20].

2.3.3 Photon sensitivity

PET image quality is directly related to the signal-to-noise ratio (SNR), which is given by

$$SNR = \frac{\mu}{\sigma}, \tag{2.6}$$

where μ is the mean signal intensity of a pixel and σ is the standard deviation of the signal fluctuation. In PET, the number of LORs detected by a certain

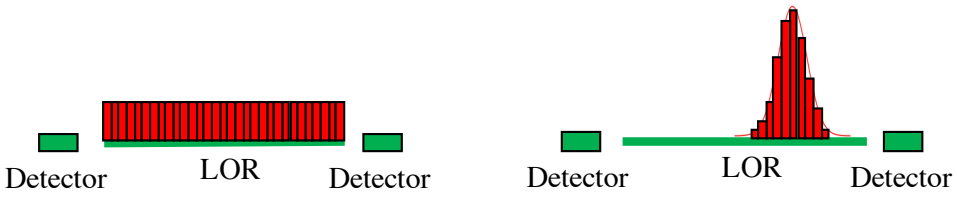

Figure 2.5: Explanation of the time of flight (TOF) technique. Left: Non-TOF, where the entire LOR is assigned equal probability of being the location of an annihilation event. Right: TOF, where the time difference between two photons are used to assign a high probability to a certain segment of LOR.

pair of detector elements over a fixed duration obeys Poisson distribution, whose standard deviation is the square root of its mean value. Because the intensity of a PET image pixel is proportional to the sum of LORs detected by all pairs of detector elements that go through it and because the detection between different pair of detector elements is independent, the pixel intensity also obeys Poisson distribution. As a result, SNR improves as the square root of the number of LORs.

An intuitive idea to improve the number of LOR is to improve the scanning time. However, considering the half life of radiotracers (for example, 109.77 minutes for ^{18}F) and the large throughput of PET scanning in hospitals, a long scanning time is not feasible. Another idea is to increase the activity of radiotracers, and thus more annihilation photons are emitted within a unit time. However, the radioactive dose to patients limits the amount of radiotracers. Increasing radioactivity also results in the increase of random coincidences, which degrades the image quality.

A more practical way to improve SNR is to improve the photon sensitivity, which refers to the ratio of detected LORs to the number of radioactive decays. Photon sensitivity can be represented as

$$Photonsensitivity = \eta_g \cdot \eta_d \cdot T, \tag{2.7}$$

where η_g is the scanner geometry efficiency, η_d is the detector intrinsic efficiency and T is the data acquisition signal threshold [21]. The geometry efficiency η_g is the ratio of annihilation photons whose paths intersect with the detecting material of a PET scanner to the total number of annihilation

photons. It is determined by the scanner configuration, which is directly related to the solid angle coverage. The intrinsic efficiency η_d refers to the ability to stop a 511 keV photon of a photon detector. The threshold T is related to the energy window (section 2.3.1) and time window (section 2.3.2). For example, a 511 keV photon may have a series of Compton scattering before the photoelectric effect, and its energy is shared by all these interactions. If none of the interactions satisfies the energy window, such a photon can not be used to constitute a coincidence event.

2.3.4 Spatial resolution

The spatial resolution of a PET system is determined by both the underlying physics principle and the instrumentation performance. The two main physics-level effects are positron range and annihilation photon acollinearity, and the foremost instrumentation-level effect is the precision for a photon detector to localize the position of interaction. Readers can find more details in [22].

Positron range refers to the distance of a positron between the point of emission and annihilation, which is determined by the initial kinetic energy of positron and the type of medium. For example, the FWHM positron range of ^{18}F is 0.102 mm in water [23]. Photon acollinearity is caused by the the residual momentum of a positron before its annihilation. The FWHM angle is about 0.5° [24]. The larger the system geometry, the worse the blurring from photon acollinearity.

The finite size of photon detector elements limits the precision to localize an interaction. As a result, the concept of an infinite thin LOR is extend to a tube of response, which has a specific width and shape. As explain in Fig. 2.6, tube of response consists of all possible connections between two detector elements. In other words, the width and shape of a tube of response is defined by the size and shape of detector elements. A small detector element is beneficial to the spatial resolution.

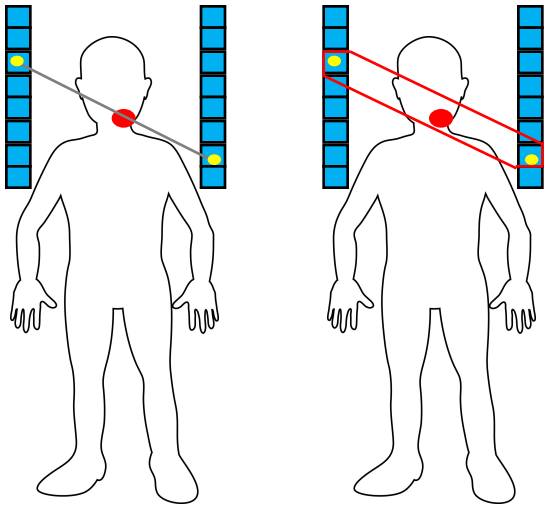

Figure 2.6: Left: line of response, which is an infinitely thin line. Right: "tube of response", which is made up by all the possible connections between two detector elements.

2.3.5 Spatial resolution uniformity

As explained in section 2.3.4, tube of response of different pair of detector element has different size and shape. For example, consider a PET system with a two-panel arrangement. In this case, detectors are able to localize interactions along the direction parallel to the panels, but can not record the position along the orthogonal-panel direction. As shown in Fig. 2.7 (2-D case for the sake of simplicity), the tube of response that is orthogonal to the panels are thinner than the tube of response that is more parallel to the panels, which results in a better spatial resolution along the parallel-panel direction. Further, the more two annihilation photons are emitted parallel to the panels, the more difficult it is for the two photons to be detected, which causes the loss of information along the parallel-panel direction.

The problem of spatial resolution uniformity also exists in a PET system with a commonly used ring arrangement. In this case, detectors can locate interactions in the angular and axial direction, but not the radial direction. As a result, the image spatial resolution degrades with increasing distance from the field of view (FOV) center, which is known as the parallax effect [25].

The nonuniformity can be mitigated by utilizing the depth of interaction (DOI) information of the photon detector, which allows photon detectors to

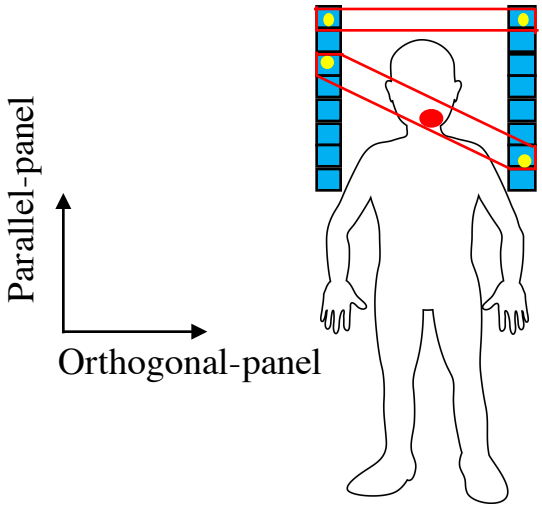

Figure 2.7: For a PET system with a two-panel arrangement, the spatial resolution along the parallel-panel direction is better than the orthogonal-direction.

measure the position of interaction in three dimensions. Equivalently, DOI capability reduces the size of detector elements and thus make a smaller tube of response, which makes images more uniform.

Chapter 3

Head-and-neck cancer dedicated PET

The need of a HNC dedicated PET system and the design of the proposed dedicated system are explained in this chapter.

3.1 Necessity of a HNC dedicated system

HNC accounts for approximately 4% of all cancers in the United States [26] and the overall annual mortality rate is 23% [27]. WB PET has been widely used for HNC diagnosis [28], recurrence prediction [29] and radiotherapy [30] because of its high sensitivity and specificity when compared with computed tomography (CT), magnetic resonance imaging (MRI), sonographic and histopathological findings [1].

The spatial resolution of WB PET is typically 4 to 6 mm [2]. For structures less than twice the reconstructed image resolution, the true amount of activity is not completely depicted [31], which causes the detection of lesions less than 10 mm in diameter less accurately. However, more than 40% of cervical lymph node metastases have been found to be present in lymph nodes smaller than 10 mm [3]. The spatial resolution of WB PET may limit the management of HNC. For example, in [32], the FDG-PET false-negative diagnosed lymph nodes ranged from 0.3 to 7.5 mm and 80% of those nodes are 5 mm in diameter or smaller.

In order to improve the head and neck imaging using WB PET, a dedicated HNC protocol is employed [33]. A dedicated HNC protocol has a longer bed time on the head and neck position, while a standard protocol consists of a midcranium to proximal thigh emission scan with a fixed bed time per bed position. Even though the dedicated protocol shows an improved sensitivity in detecting small lymph nodes and cervical node metastases (smaller than 15 mm), it still yields false-negative findings and fails to detect some malignant

lymph nodes when the lesion size is in the range of 5 to 10 mm, and the specificity for lymph node metastases detection gets lower [34].

HNC needs special attention because the goal of HNC treatment is not only to improve survival outcomes but also to preserve organ function, which is due to the complex anatomy and vital physiological role of the tumor-involved structures [35]. A higher spatial resolution image with a better contrast will allow radiation oncologists to accurately design planned target volume dose, detect smaller sized lymph nodes and identify the boundaries of tumors, which provides more freedom to choose the treatment options including surgery, radiation therapy, chemotherapy, and targeted therapy, with an improved consideration of how the treatment affects the quality of life of patients. For example, limited nodal disease can often be treated surgically with radical neck dissection, while more extensive nodal disease may require adjuvant radiation therapy in addition to surgery [36]. Thus, a HNC dedicated PET system that considers the spatial imaging environment of HNC is needed for a better diagnosis and treatment.

3.2 System design

Previous organ-dedicated PET systems mainly focuses on brain and breast, which is summarized in Table 3.1. As a comparison, Table 3.2 summarizes some recently published commercial WB PET systems.

Comparing Table 3.1 and Table 3.2, some differences between dedicated PET systems and WB PET systems are noticeable. The first discrepancy is system geometry. While WB PET systems are all designed with a ring structure to adapt to different regions of the body, dedicated PET systems have various system geometries, taking the specific imaging environment into consideration. For example, breast PET systems prefer a two-panel geometry, while a helmet geometry are commonly utilized in brain PET systems. The purpose of using a special system geometry is to improve the solid angle

[1]For scintillators, show the crystal element size. For semiconductors, show the intrinsic spatial resolution. Unit: mm.

[2]Use the best investigated FWHM value. Unit: mm.

[3]Position-sensitive avalanche photodiode.

[4]Position-sensitive photomultiplier.

[5]Digital silicon photomultiplier.

Table 3.1: Summary of some previously studied organ-dedicated PET systems.

System	Organ	Geometry	Crystal	Crystal size[1]	Detector	DOI[2]
[37]	Breast	Two panels	LSO	$2 \times 2 \times 20$	APD	2
[38]	Breast	Two panels	LSO	$1 \times 1 \times 3$	PSAPD[3]	3
[39]	Breast	Two panels	CZT	< 1	–	2
[40]	Breast	Two panels	LYSO	$1.88 \times 1.88 \times 15$	PSPMT[4]	no
[41]	Breast	Box	LSO	–	SiPM	yes
[42]	Brain	Helmet	LSO	$2.5 \times 2.5 \times 20$	–	yes
[43]	Brain	Helmet	GSO	$2.8 \times 2.8 \times 7.5$	PMT	yes
[44]	Brain	Ring	LYSO	$1.5 \times 1.5 \times 10$	SiPM	no
[45]	Brain	Helmet	LYSO, $LaBr_3$	$1 \times 1 \times 3$	SiPM	yes

Table 3.2: Summary of some recently published commercial WB PET systems.

System	Geometry	Crystal	Crystal size[1]	Detector	DOI[2]
Philips Ingenuity TF[46]	Ring	LYSO	4×4×22	PMT	no
Siemens Biograph mCT[47]	Ring	LSO	4×4×20	PMT	no
GE Discovery 690[48]	Ring	LYSO	$4.2 \times 6.3 \times 25$	PMT	no
Philips Vereos Digital[49]	Ring	LYSO	4×4×19	dSiPM[5]	no
Toshiba Celesteion[50]	Ring	LYSO	4×4×12	PMT	no

coverage of the interested imaging region, and thus increase the photon sensitivity. Second, the crystal size of dedicated PET system are smaller than that used in WB PET systems, which helps to improve the spatial resolution as discussed in section 2.3.4. Third, to achieve a higher spatial resolution than WB PET systems, dedicated PET systems tend to implement the DOI capability at the cost of a more complicated detector design. Fourth, for some dedicated PET system inserted to other imaging modalities such as CT or MRI, the system dimension is important. SiPM is smaller than PMT and gets more applications in the dedicated PET systems.

There also exists common features between WB and dedicated PET systems. Compared with semiconductor, scintillator dominates the detecting materials. Among all different scintillators, LYSO shows a balanced performance in terms of large cross section, high light output, small decay time [51] and it has been widely used in commercial PET systems. For semiconductor, however, only CdTe and CZT has been used to fabricate PET systems. Compared with CdTe/CZT, LYSO has advantages including:

- a higher effective atomic number and density and thus a larger detection efficiency;
- a lower cost;
- a larger photoelectric-to-Compton cross section ratio.

At the same time, the disadvantage of a LYSO detector includes:

- a lower energy resolution;
- a inferior intrinsic spatial resolution.

Based on Table 3.1 and Table 3.2, LSO and LYSO are the mainstream choice.

Based on the previous study, the HNC dedicated PET system was designed as follows. The system was made up of two panels, the distance between which could be adjusted to get in close proximity to patients neck to improve photon sensitivity without blocking patients eyes. Considering the human head and neck size [52], the panel size was designed as $243 \times 243\ mm^2$. The detecting material was LYSO for its high density, high effective atomic number, low cost and high light output [53]. Considering the tradeoff between a better spatial resolution and the crystal segmentation cost, the crystal size

was $2 \times 2 \times 20\ mm^3$. The proposed system is shown in Fig. 3.1. This system is modeled in GATE (Geant4 Application in Tomographic Emission) [54] and its performance is evaluated in the next chapter.

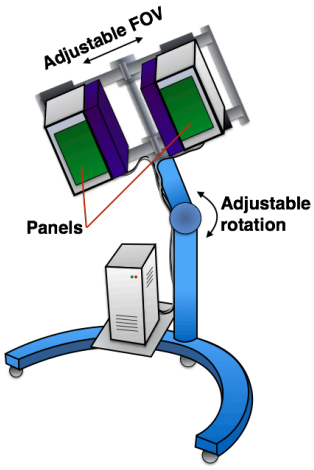

Figure 3.1: Schematic diagram of the two-panel HNC dedicated PET system. The two panels are positioned by the patients' shoulders and adjusted close to the patient's head while the patient lies down in the whole body scanner.

Chapter 4

System performance

To investigate the system performance, a Monte Carlo simulation was performed in GATE [54]. Specifically, the system performance includes: (1) NEC rate; (2) photon coincidence sensitivity within the FOV; (3) spatial resolution and DOI influence; (4) multiple scattering events recovery efficiency and recovery correct rate; (5) hot rods visualization capability in terms of SNR and contrast-to-noise ratio (CNR).

In the simulation, the panel distance was set as 200 mm and the gap between two neighboring crystal was 0.2 mm. Based on the detector performance of former brain-dedicated PET systems made up of SiPM and segmented LYSO [55, 56], the energy resolution of the proposed system was assumed to be 10% full-width at half maximum (FWHM) at 511 keV and the time resolution was set as 400 ps FWHM. The system noise level was set as 50 keV, which means an interaction was discarded if its energy deposition was less than 50 keV.

The performances of the proposed system were compared with a state-of-the-art commercial WB PET system - GE Discovery MI (3-ring configuration, 150 mm axial FOV, 744 mm diameter bore). According to [57], the crystal size is 3.95 mm (transaxial), 5.3 mm (axial), and 25 mm (radial), the average photo peak energy resolution is 9.40% FWHM, and the average coincidence time resolution is 375.4 ps FWHM. The optimized energy window and time window was set as 425 - 650 keV and 4.9 ns respectively.

4.1 Noise equivalent count (NEC) rate

The NEC [58] rate incorporates the noise effects of random and scatter count and is an indicator of the SNR for PET system, which is calculated as

$$NEC = \frac{T^2}{T + S + R}, \tag{4.1}$$

where T, S and R are true, scattering and random coincidence event rates, respectively.

For HNC PET scanning using non-specific tracers such as FDG, background activity mainly comes from the brain and torso, and a simplified model was used to mimic the geometry. For head and neck, a cylinder phantom with a 110 mm diameter and 126 mm height was used and the concentration activity was 5.7 kBq/cm^3 [33]. The brain was modeled as a 130 mm diameter and 80 mm height cylinder, while the torso was simplified as a 260 mm diameter and 200 mm height cylinder. The concentration activity ratio of head and neck, brain, and torso was set as 1:8:1 and water was used as the cold background. Five time-windows (0.4 ns, 1 ns, 2 ns, 4 ns, 6 ns) and five energy-windows ([491, 531] keV, [461, 561] keV, [421, 601] keV, [381, 641] keV, [341, 681] keV) were studied and the working windows were chosen under which the NEC rate reached the maximum value. Random coincidence can be reduced by shielding the detector, which helps to improve the NEC rate. To investigate the benefits of shielding, two 20 mm thickness and 30 mm width lead strips were placed on the head side and torso side of the two panels. The weight of each lead strip was 1.65 kg. Simulation configurations are shown in Fig. 4.1, and each configuration had about 2M coincidence events.

The data processing are described as follows. Raw data GATE Hits file contained time, energy, position, and eventID information of every interaction, and all these information were precise. However, to mimic the finite detecting capability of detectors, time and energy of every interaction were blurred with a Gaussian distribution, and the standard deviation σ was calculated as

$$\sigma = \frac{FWHM}{2.355}, \tag{4.2}$$

where $FWHM$ was the time resolution and energy resolution. In reality, if the time interval between two interactions that happen within one crystal is

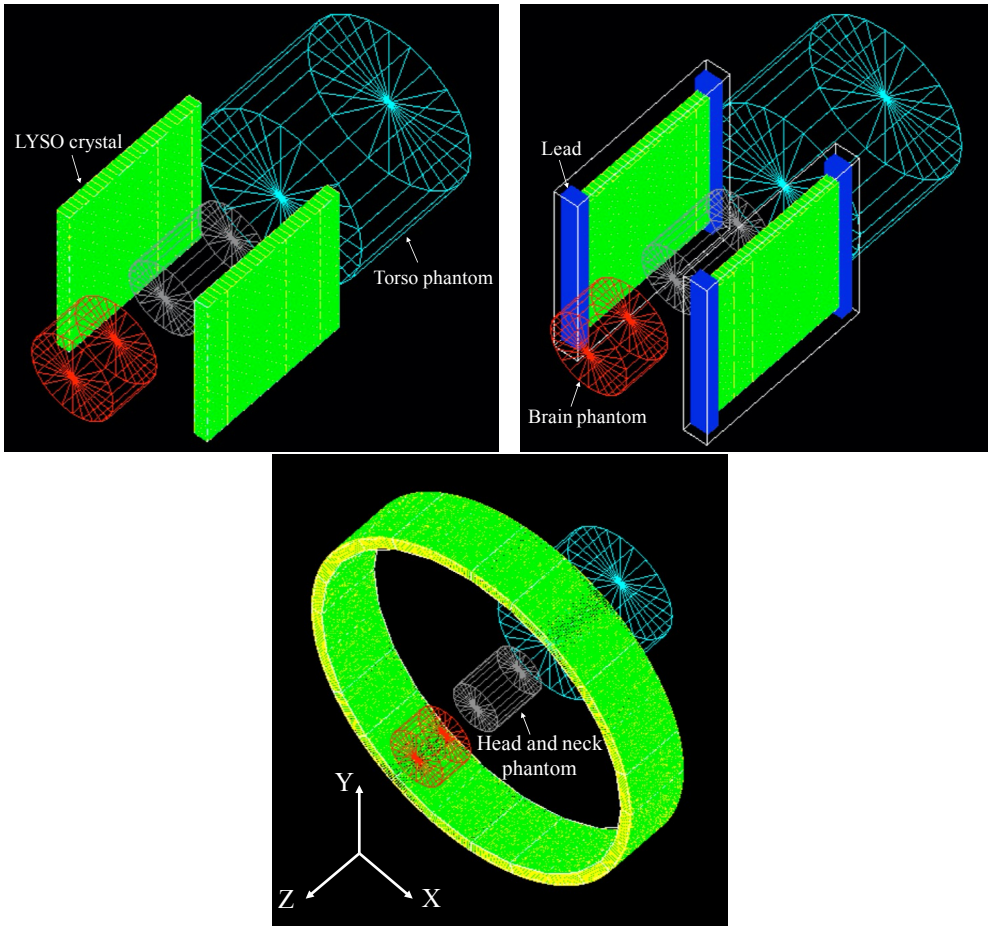

Figure 4.1: The simulation model for NEC rate study. Left: the dedicated system without lead shielding. Middle: the dedicated system with lead shielding. Right: The GE Discovery MI whole body PET system. Green is detector, blue is lead shielding, red is brain, grey is head and neck and cyan is torso. Coordinate system is also shown.

too small, the detector may not be able to distinguish them and read them out as one signal instead. As a result, interactions had took place in the same single crystal within 1.4 ns ($6\sqrt{2}\sigma$) were combined into one new interaction, whose energy was the sum of original interactions, and time and position of interaction were energy weighted. If all the original interactions shared one eventID, the combined interaction was also marked with the same eventID, otherwise the new eventID would be set as 0. Two interactions occurring within a selectable energy and time window were chosen as a coincidence event. For the coincidence events, if two interactions had the same eventID and neither of them scattered within the phantoms before reaching the de-

tector, they were considered a true coincidence (T). If two coincidences had the same eventID but either or both scattered within the phantoms, they were assigned as a scattered coincidence (S). If two coincidences did not have the same eventID, they were treated as a random coincidence (R).

NEC rate and total count rate are shown in Fig. 4.2. For the dedicated system without lead shielding, NEC rate reached the maximum value of 9.3 $kcps$ at 5.7 kBq/cm^3 with the 1 ns time window and the [461, 561] keV energy window, under which the total count rate was approximately 26.8 $kcps$. After adding the shielding, maximum NEC rate increased to 10.5 $kcps$ at 5.7 kBq/cm^3 with the same time window and energy window, and the total count rate decreased to 25.8 $kcps$. With the shielding, the maximum NEC rate had a 12.9% improvement and the maximum total count rate reduced to 3.7%. As a comparison, the WB PET system had a 1.0 $kcps$ NEC rate and a 17.5 $kcps$ total count rate with the same phantom and simulation time. Comparing the two systems, the NEC rate peak of the dedicated system with or without lead shielding were 9.5 and 8.3 times higher than that of the WB system, which is about one order of magnitude improvement.

The peak NEC rate for the GE Discovery MI was 1.0 $kcps$ at 5.7 kBq/cm^3, which is about two orders of magnitude smaller than the reported value of 100 $kcps$ at 20.6 kBq/ml [2]. Two factors may be contributing to the difference. The first factor is the different total activity in the phantom used for the NEC rate measurement. In our study the total activity in the head and neck phantom was 6.8 MBq, while in [2] the activity was 109 MBq, which is about 16 times larger. The second factor is the different phantom configuration. In our study, the specific HNC imaging environment was considered and high background activity from brain and torso caused a relatively low NEC rate, while Ref. [2] used the standard NEMA phantom for the NEC rate study. Our results showed that the dedicated system was more specific for HNC than the WB PET system.

Random coincidence event rate was the main limitation of NEC rate of the dedicated system, which was caused by the compact geometry of the dedicated system. As explained in Ref. [59], for a cylindrical PET system with radius r, the true coincidence rate is proportional to $1/r$, while the random coincidence rate is proportional to $1/r^2$. To reduce the random coincidence rate, a narrower energy window is necessary, which requires a higher energy resolution of the system.

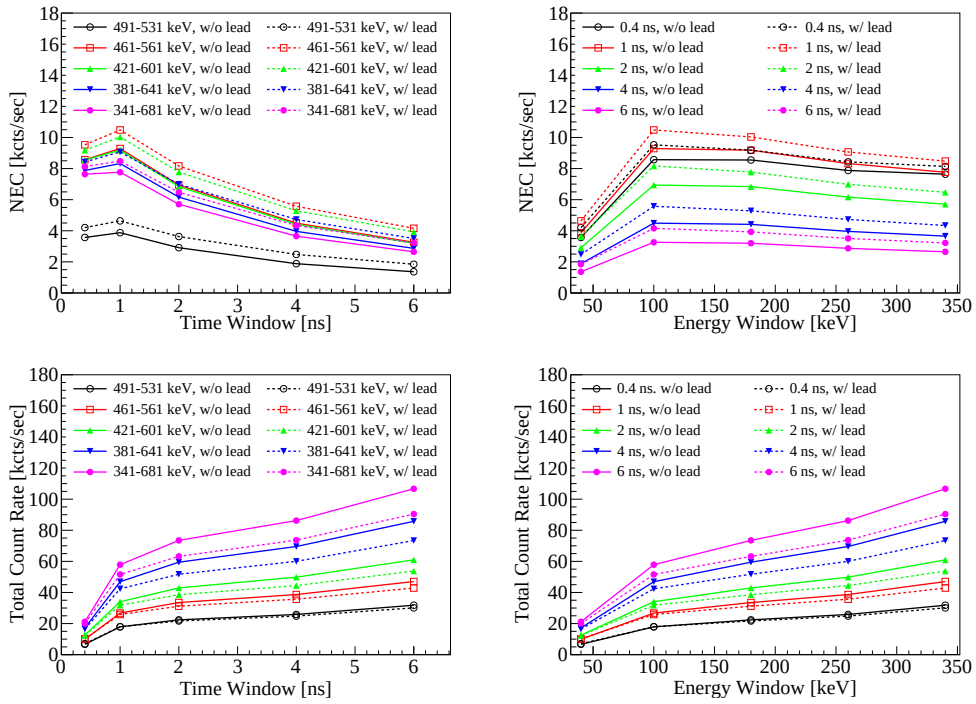

Figure 4.2: The NEC rate (the top row) and total count rate (the bottom row) of the dedicated system for different time windows and energy windows. Without shielding, maximum NEC rate is 9.3 *kcps* at 5.7 kBq/cm^3 under 1 *ns* time window and [461, 561] *keV* energy window, and the corresponding total count rate was about 26.8 *kcps*. With shielding, maximum NEC rate of 10.5 *kcps* at 5.7 kBq/cm^3 is achieved with the same time window and energy window, and the corresponding total count rate was about 25.8 *kcps*.

4.2 Photon sensitivity

The photon sensitivity was defined as the ratio of the total photon coincidence count rate to the source activity. A point source with a activity of 7 MBq was used for the sensitivity study [33]. No lead shielding was used for the sensitivity study. To understand the sensitivity uniformity within the FOV, the point source was placed at 9 places within the FOV, which are the FOV centre, off centre 20, 40, 60, 80 *mm* along the direction parallel (Z&Y axes in Fig. 4.1) to the panel, and 20, 40, 60, 80 *mm* orthogonal (X axis in Fig. 4.1) to the panel. Each position had the same simulation duration and got approximately 2M coincidence events. The time and energy windows were based on the result in section 4.1. The system sensitivity was compared with

the GE Discovery MI.

The photon sensitivities of the dedicated PET system and the WB PET are shown in Fig. 4.3. For the dedicated system, the maximum sensitivity is 0.83% at the FOV centre. For the WB system, the maximum sensitivity is 0.61% at the FOV centre. The reported sensitivity of GE Discovery MI is 7.5 cps/kBq [2], which is in agreement with the simulation result. It was shown that the sensitivity of the dedicated system was approximately the same as other commercial whole body clinical PET systems (about 1-2% at the FOV center). The result suggested that the two-panel geometry compensated the benefits of the compact system design. However, the simulation results still showed that the dedicated system had a 36.1% higher sensitivity than a state-of-the-art WB PET for a point source placed at the FOV center.

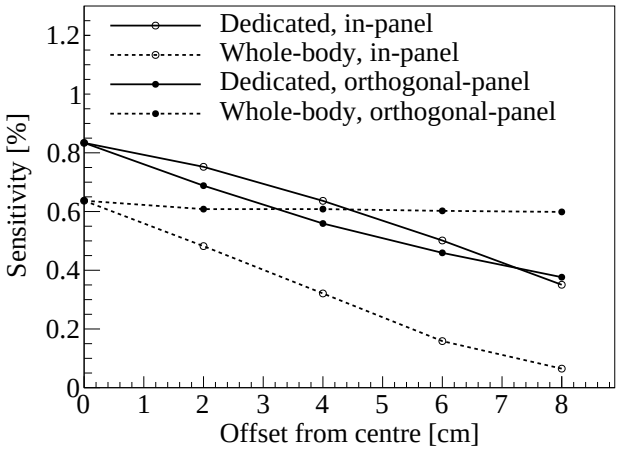

Figure 4.3: The photon sensitivity of the dedicated system (solid lines) and the WB system (dotted lines). A 7 MBq point source was shifted along the parallel-panel direction and orthogonal-panel direction.

4.3 Spatial resolution

The spatial resolution can be represented as the diameter of spheres that the system can resolve. The smaller the diameter is, the better the system spatial resolution is. To investigate the minimum sphere size that the dedicated system could resolve, three sets of hot sphere sources were placed along the parallel-panel direction and the orthogonal-panel direction. In each set,

the sphere diameters were 1, 1.5 and 2 mm, and the distance between two neighboring spheres was twice the diameter.

Image was reconstructed with a TOF list-mode 3D MLEM image reconstruction algorithm [11] through *gpurecon* program [60]. The interaction was assumed to take place on the central axis of crystals, while a Gaussian distribution was used to blur the position of interaction along the direction of depth to investigate the influence of DOI resolution on the spatial resolution. Different DOI resolution 0, 2, 4, 6 mm FWHM were studied, and the σ of Gaussian distribution was calculated by equation (4.2). In the reconstruction, the FOV was $160 \times 160 \times 160$ mm^3 and the voxel size was $1 \times 1 \times 1$ mm^3.

The reconstructed image is shown in Fig. 4.4. In each figure, the FOV centre is in the top-left corner. The horizontal direction is the orthogonal-panel direction and the vertical direction is the parallel-panel direction. Based on the result, given a specific sphere diameter and a DOI resolution, the reconstructed spheres along the vertical direction were more distinguishable than the spheres along the horizontal direction, which meant the dedicated system had a higher parallel-panel spatial resolution than the orthogonal-panel spatial resolution. With the deterioration of DOI resolution, both the parallel-panel and orthogonal-panel spatial resolution deteriorated, and the reconstructed spheres gradually became ellipses, which suggested that orthogonal-panel was more sensitive to DOI resolution. For the dedicated system, 1 mm parallel-panel and 1.5 mm orthogonal-panel spatial resolution was achievable when DOI resolution was 2 mm FWHM.

The difference between the parallel-panel and the orthogonal-panel spatial resolution was due to the limited angle tomography of the two-panel geometry, which caused the incomplete angular sampling. Specifically, a pair of photons emitted approximately parallel to the panels were not likely to be detected, and spatial information along orthogonal-panel direction was missing. DOI information could help to reduce the difference between the parallel-panel and the orthogonal-panel spatial resolutions.

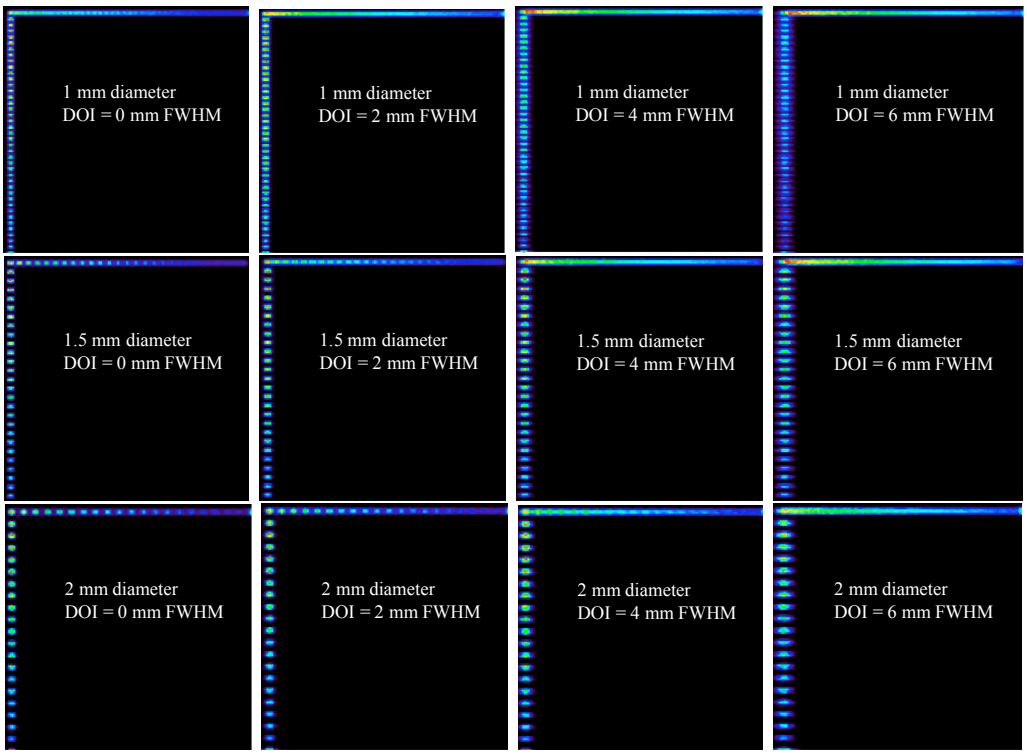

Figure 4.4: The reconstructed image for resolving spheres. In each figure, the FOV centre is in the top-left corner. Horizontal direction is the orthogonal-panel direction and vertical direction is the parallel-panel direction. With a 2 mm DOI resolution FWHM, 1 mm parallel-panel and 1.5 mm orthogonal-panel spatial resolution was achievable.

4.4 Compton recovery

Multiple scattering events that are normally discarded have been recovered using different methods to improve the system sensitivity [61, 62, 63, 64], which helps to improve the SNR to facilitate the reconstruction of a high resolution image and reduce the scanning time. The key point in recovering multiple scattering events is to identify the first interaction of primary photons (511 keV photons created by the annihilation of a positron), which keeps the position information of the original annihilation when forming a LOR.

Annihilation photons were classified based on their interaction sequences. For example, a photon that only had a photoelectric event was denoted as a P photon, while a photon that had one Compton scattering before the photoelectric event was denoted as a CP photon. The coincidence between

two P photons was called a P-P coincidence, while the coincidence between one P photon and one CP photon was called a P-CP coincidence. In this initial study, only P-CP coincidences were recovered.

The selection of P-CP coincidences was similar to that of P-P coincidences, except that in each time window three interactions were selected, in which one interaction was detected by one panel, and the other two interactions were detected by the second panel. The total energy deposition in each panel should fall in the energy window.

In a P-CP coincidence, there are three detected interactions, one of which belonged to a P photon, and the other two belonged to a CP photon. The P photon could be easily distinguished because its panel only had one interaction. For the CP photon, however, which interaction was the Compton scattering was not clear. Thus, the direction difference angle (DDA) method [61] was used to identify the Compton scattering in a CP photon.

In a Compton scattering, the scatter angle is the angle between the incident photon and the scattered photon, which can be written as

$$\theta_P = \cos^{-1}\left(\frac{\overrightarrow{V_i} \cdot \overrightarrow{V_s}}{|\overrightarrow{V_i}| \cdot |\overrightarrow{V_s}|}\right), \tag{4.3}$$

where $\overrightarrow{V_i}$ and $\overrightarrow{V_s}$ are the vectors of incident and scattered photons. At the same time, based on Compton kinematics, the scattering angle and the energy of the scattered photon have a one-to-one correspondence. Thus, the scattering angle can also be calculated as

$$\theta_E = \cos^{-1}(1 - m_0c^2(\frac{1}{E_s} - \frac{1}{E_i})), \tag{4.4}$$

where E_i is the energy of the incidence photon, E_s is the energy of the scattered photon and m_0c^2 is the rest mass of an electron. For PET application, $E_i = m_0c^2 = 511\ keV$. A θ can also be acquired through the position of interaction information.

For a CP photon, the two interactions were assumed as the Compton scattering respectively, and two sets of θ_P and θ_E were calculated. Ideally, in the correct assumption, θ_P was equal to θ_E, while in the incorrect assumption they were different. However, due to the finite spatial resolution and energy resolution, θ_E and θ_P had error and differences existed even in the correct

assumption. In the DDA method, the correct sequence was determined by a smaller $\theta_{DDA} \equiv |\theta_E - \theta_p|$. The DDA method is depicted in Fig. 4.5.

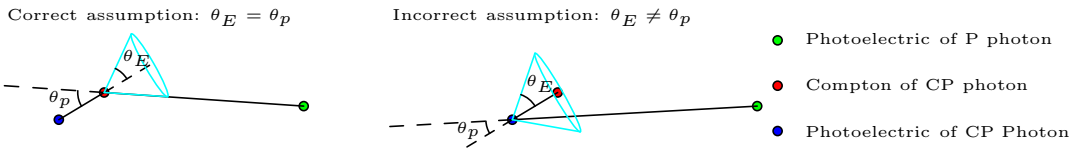

Figure 4.5: The direct difference angle method is used to identify the Compton scattering in a CP photon. By assuming the two interactions within a CP photon as the Compton scattering respectively, two sets of θ_E and θ_p were calculated. The assumption under which $\theta_{DDA} \equiv |\theta_E - \theta_p|$ is smaller is selected.

The system sensitivity improvement due to the recovered scattering events and the *recovering-correct-rate* will affect the image quality. The sensitivity improvement was defined as the ratio of number of P-CP coincidences to the number of P-P coincidences, and the *recovering-correct-rate* was defined as the ratio of correctly identified P-CP coincidences to the total P-CP coincidences. To investigate the trade-off between the two factors, a threshold $|\theta_{E_c} - \theta_{E_i}|$ was used to select P-CP coincidences, where θ_{E_c} and θ_{E_i} were θ_E under the correct and incorrect interaction sequences. Given a threshold, only the P-CP coincidences whose $|\theta_{E_c} - \theta_{E_i}|$ were larger than the predefined threshold would be selected, and the *recovering-correct-rate* was calculated based on the selected coincidences.

The dependence of the sensitivity improvement and the *recovering-correct-rate* on the threshold $|\theta_{E_c} - \theta_{E_i}|$ is shown in Fig. 4.6. The error bars shows the standard deviation among the 9 data sets. With a larger threshold, the sensitivity improvement kept decreasing, while the *recovering-correct-rate* kept increasing, which showed the trade-off. When the threshold was 0°, the maximum sensitivity improvement was 225.3%.

Three thresholds 0°, 75°, 115°, which corresponded to approximately 60%, 80% and 90% *recovering-correct-rate*, were chosen to show the sensitivity improvement at different positions within the FOV, which is shown in Fig. 4.7. The approximately horizontal shape suggested that the sensitivity improvement is relatively uniform within the FOV, and thus multiple scattering events recovery would not distort the original concentration activity ratio within patients' body.

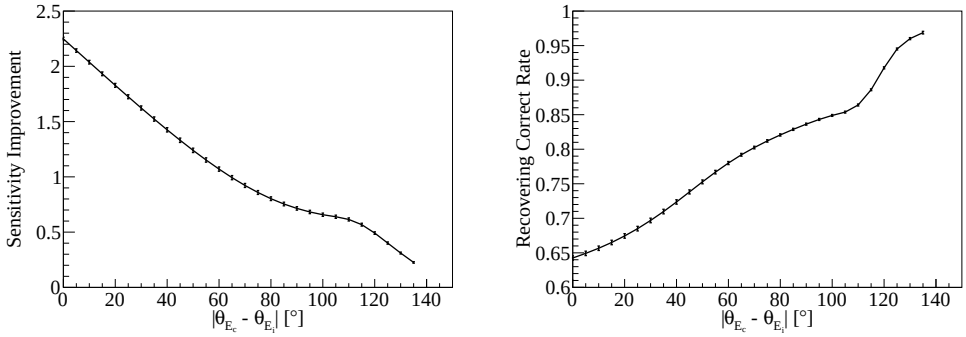

Figure 4.6: The dependent relationship of the sensitivity improvement (left) and the *recovering-correct-rate* (right) as a function of P-CP coincidence selection threshold $|\theta_{E_c} - \theta_{E_i}|$. The error bars show the standard deviation among the 9 data sets.

4.5 Hot rod visualization

For the hot rod visualization study, the head and neck phantom model in section 4.1 was used. Four hot rods whose diameters were 1, 2, 3 and 4 mm were put 14 mm away from the phantom centre. The concentration activity of the hot rods and the cold background was 8:1 [33]. The same phantom were both simulated with the dedicated system without lead shielding and the WB system. Each configuration had 140 s simulation time. The number of P-P coincidences of the dedicated system and the WB system were 2.73M and 1.79M respectively. For the dedicated system, the DOI resolution was set as 2 mm FWHM. The image reconstruction algorithm was TOF MLEM without normalization. For the dedicated system, the voxel size was $1 \times 1 \times 1\ mm^3$, while that of the WB system was $2 \times 2 \times 2\ mm^3$.

Image quality quantified by SNR and CNR were used to compare the WB system and the dedicated system. *Contrast* of a given hot rod was defined as [65]

$$contrast = \frac{C_{rod} - C_{bkg}}{C_{rod}}, \tag{4.5}$$

where C_{rod} is the average voxel value within the hot rod and C_{bkg} is the average voxel value of the background. Here the background was acquired from four rods that were faraway from the hot rods. The SNR was defined as [65]

$$SNR = contrast \times \frac{C_{bkg}}{\sigma_{bkg}}, \tag{4.6}$$

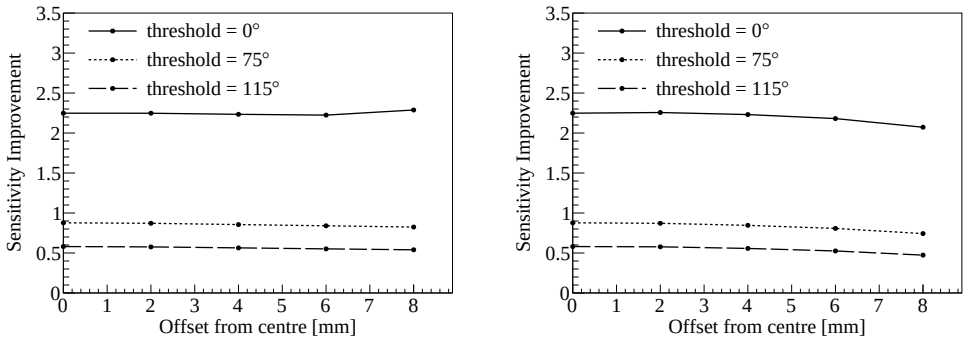

Figure 4.7: The system improvement at different position within the FOV. It shows the sensitivity improvement to be relatively uniform within the FOV. Left: sensitivity improvement along the parallel-panel direction. Right: sensitivity improvement along the orthogonal-panel direction.

where σ_{bkg} is the standard deviation of the average voxel value of the four background rods. CNR was defined as [66]

$$CNR = \frac{C_{rod} - C_{bkg}}{\sigma_{bkg}}. \tag{4.7}$$

CNR and SNR were used to investigate the feasibility of Compton recovery of the dedicated system and to understand the trade-off between the sensitivity improvement and the *recoverying correct rate*. P-CP coincidences under different thresholds (0°, 30°, 50°, 75°, 95° and 115°) were incorporated with P-P coincidences to reconstruct images.

The dependence of SNR and CNR of reconstructed image based on both P-P coincidences and P-CP coincidences on the threshold $|\theta_{E_c} - \theta_{E_i}|$ is shown in Fig. 4.8. As the threshold was increased, thus increasing the *recovering-correct-rate*, SNR and CNR kept decreasing for all four rods. The reconstruction algorithm assumes Poisson distribution of positron annihilation and photon detection, thus the counts of a voxel should be the square of its standard deviation. According to equation 4.6 and 4.7, voxel counts appear in the numerator and voxel standard deviation appears in the denominator, which explains why the sensitivity improvement dominated the quality of reconstructed image in terms of SNR and CNR. The results suggest that all the recovered P-CP coincidences should be used for image reconstruction.

The reconstructed image for lesion visualization is shown in Fig. 4.9. For the image of the dedicated system based on both P-P coincidences and P-

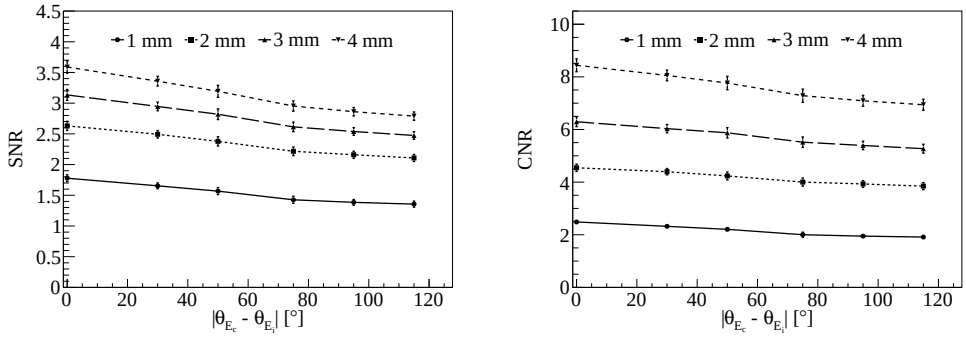

Figure 4.8: The dependence of SNR and CNR of reconstructed image based on both P-P coincidences and P-CP coincidences on the threshold $|\theta_{E_c} - \theta_{E_i}|$. The legend refers to the 4 hot rods. As the threshold is increased, SNR and CNR kept decreasing.

CP coincidences, no threshold was set to select P-CP coincidences. The *recovering-correct-rate* was 64.7% and the system sensitivity improvement was 225.3%. The images are displayed using the same intensity scale. Figure 4.9 shows that the 2, 3 and 4-*mm* diameter lesions could be visualized by the dedicated system, and the 2-*mm* lesion became more noticeable after recovering P-CP coincidences. As a comparison, the WB system can only resolve the 3 and 4-*mm* diameter lesions, and the 3-*mm* lesion was blurred. Given the hot-to-background concentration activity ratio (8:1) and simulation time (140 *s*), the dedicated system could not resolve the 1-*mm* lesion, which could be caused by the bad orthogonal-panel spatial resolution and mismatch of round rod and square voxel.

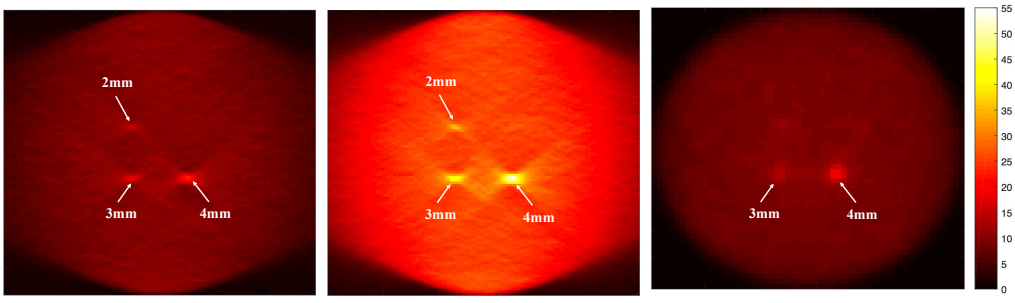

Figure 4.9: The reconstructed image for lesion visualization. Arrows point to the hot rods. Left: dedicated system images based on P-P coincidences. Middle: dedicated system image based on P-P and P-CP coincidences. Right: whole-body system images based on P-P coincidences.

The elliptical lesion, elliptical phantom contour and the artifact on the left and right sides of lesions of the dedicated system pointed to the limited angle problem, which was also reported in previous stationary two-panel designs [38, 39], where the authors tried to alleviate the problem by improving hardware performance such as a higher DOI resolution. We propose a different solution for our system. As explained before, the dedicated system is supposed to replace the dedicated HNC protocol within a standard WB PET protocol, and the images based on the WB PET can be treated as a priori information. For example, the high parallel-panel spatial resolution can be properly used to show a clear boundary of lesions.

The image qualities in terms of SNR and CNR are shown in Fig. 4.10. Compatible with the reconstructed image shown in Fig. 4.9, the SNR and CNR of the dedicated system were higher than those of the WB system, which suggested the dedicated system had a better lesion visualization ability. The SNR and CNR further improved after incorporating P-CP coincidences, which verified the benefits of recovering multiple scattering events. Due to the improved NEC rate, photon sensitivity, and spatial resolution, the proposed system exhibited a better lesion visualization than the WB system in our study. Moreover, the simulation time (140 s) was much smaller than the scanning time of a standard whole body PET scanner (30-60 min for detection of 5-10 mm diameter lesions) [67].

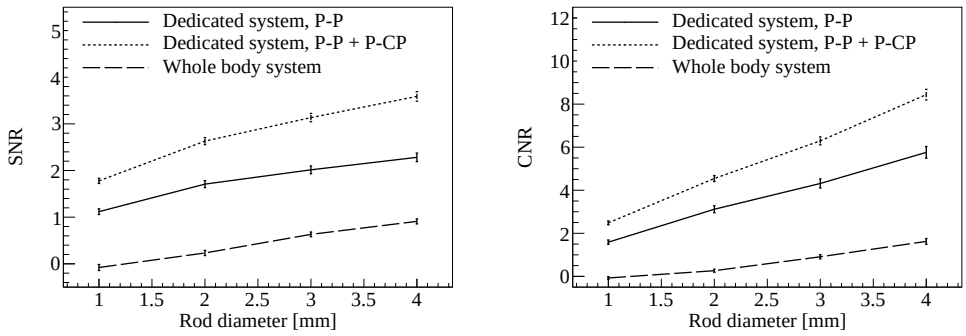

Figure 4.10: The signal-to-noise ratio (SNR) and contrast-to-noise ratio (CNR) of the reconstructed image of the head and neck phantom. For the same phantom and same simulation time, the SNR and CNR of the dedicated system is better than those of the whole body system, and incorporating P-CP coincidences further improves SNR and CNR.

Chapter 5

Conclusions & Future Work

Based on the recognition of current limitations of head-and-neck cancer diagnosis and treatment and previous organ-dedicated PET systems, this thesis proposed the design of a HNC dedicated PET system and the system performance was studied through a Monte Carlo simulation. The proposed system shows a superior performance than a cutting-edge WB PET system GE Discovery MI in terms of NEC rate, photon sensitivity, spatial resolution and lesion visualization.

Specifically, the NEC rate peak is about 9.3 $kcps$ at 5.7 kBq/cm^3, and it increases to 10.5 $kcps$ with lead shielding. The photon sensitivity is 0.83% for a point source placed in the FOV centre. With a 2 mm FWHM DOI resolution, the system achieves 1 mm orthogonal-panel and 1.5 mm parallel-panel spatial resolution. Multiple scattering events were recovered with the purpose of improving image quality and reducing scanning time. For lesion visualization, the dedicated system can visualize a 2 mm diameter hot rod, and SNR and CNR of the reconstructed image are further improved after incorporating multiple scattering events.

To validate the simulation results, a high intrinsic spatial resolution detector module with DOI capability is being developed in our lab. Customized LYSO crystal produced by EPIC-Crystal (China) is being used, SiPM is S13361-3050AE from Hamamatsu (Japan) and readout electronics is from PETSYS Electronics (Protugal). The detector module will be further scaled up to build the system in the future.

Appendix A

GATE Hits file in ROOT format

GATE can have different types of output format including ASCII, binary, ROOT and so on. ROOT is a modular scientific software framework developed by CERN and it provides all the functionality needed to handle and analysis large amounts of data in a very efficient way. In this study, all the data analysis were performed in ROOT.

Fig. A.1 shows the GATE Hits file in ROOT format. A class called 'TTree' is used to store the data, which contains many branches and each branch represents one feature of an interaction. Every time an interaction happens, all of it features are filled into the corresponding branch. The meanings of some branches are shown in Table A.1.

Table A.1: Summary of some previously studied organ-dedicated PET systems.

Branch	Meaning
PDGEncoding	Geant4 code of the particle which has generated the hit
trackID	ID of the particle which has generated the hit
parentID	ID of the mother of the particle which has generated the hit
time	Time stamp of the hit
edep	Energy deposited by the hit
stepLength	Range of particle which has generated the hit
posX	X position of the hit in the world referential
posY	Y position of the hit in the world referential
posZ	Z position of the hit in the world referential
localPosX	X position of the hit in the local referential
localPosY	Y position of the hit in the local referential
localPosZ	Z position of the hit in the local referential
gantryID	ID of volume attached to the "base" level of the system
rsectorID	ID of volume attached to the "rsector" level of the system
moduleID	ID of volume attached to the "module" level of the system
submoduleID	ID of volume attached to the "submodule" level of the system
crystalID	ID of volume attached to the "crystal" level of the system
layerID	ID of volume attached to the "layer" level of the system
photonID	ID of the photon giving the particle which has generated the hit
nPhantomCompton	Number of Compton interactions in phantoms before reaching the detector
nPhantomRayleigh	Number of Rayleigh interactions in phantoms before reaching the detector
primaryID	ID of the primary particle whose descendant generated this hit
sourceID	ID of the source which emitted the primary particle
eventID	ID of the event
runID	ID of the run (i.e. time-slice)
processName	Name of the process which has generated the hit

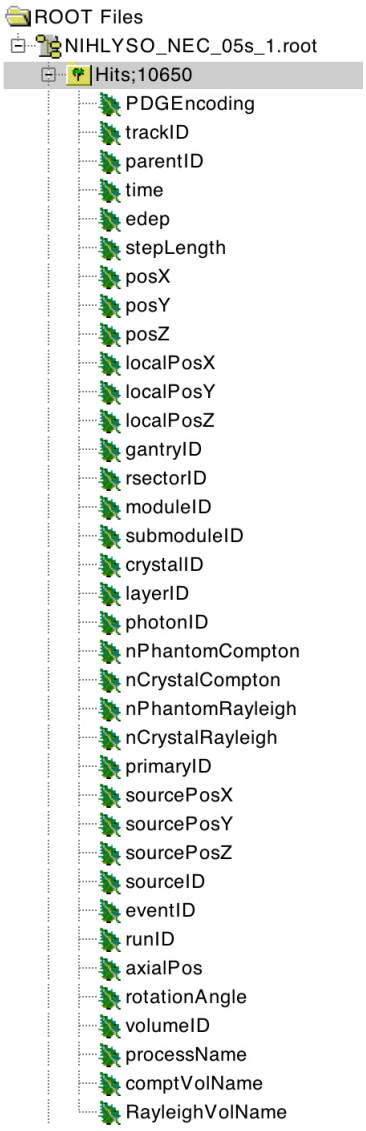

Figure A.1: The GATE Hits file in ROOT format.

References

[1] S. Adams, R. P. Baum, T. Stuckensen, K. Bitter, and G. Hör, "Prospective comparison of 18 F-FDG PET with conventional imaging modalities (CT, MRI, US) in lymph node staging of head and neck cancer," *European Journal of Nuclear Medicine and Molecular Imaging*, vol. 25, no. 9, pp. 1255–1260, 1998.

[2] C. Levin, W. Peterson, S. Ross, C. Stearns, and J. Uribe, "PET performance as a function of axial field of view for a new silicon photomultiplier-based whole body TOF PET/CT system," *Journal of Nuclear Medicine*, vol. 57, no. supplement 2, pp. 200–200, 2016.

[3] M. Van den Brekel, H. Stel, J. Castelijns, J. Nauta, I. Van der Waal, J. Valk, C. Meyer, and G. Snow, "Cervical lymph node metastasis: assessment of radiologic criteria." *Radiology*, vol. 177, no. 2, pp. 379–384, 1990.

[4] J. J. Vaquero and P. Kinahan, "Positron emission tomography: current challenges and opportunities for technological advances in clinical and preclinical imaging systems," *Annual review of biomedical engineering*, vol. 17, pp. 385–414, 2015.

[5] W. Wadsak and M. Mitterhauser, "Basics and principles of radiopharmaceuticals for pet/ct," *European journal of radiology*, vol. 73, no. 3, pp. 461–469, 2010.

[6] E. Pauwels, M. Ribeiro, J. Stoot, V. McCready, M. Bourguignon, and B. Maziere, "Fdg accumulation and tumor biology," *Nuclear medicine and biology*, vol. 25, no. 4, pp. 317–322, 1998.

[7] E. A. Rodriguez, Y. Wang, J. L. Crisp, D. R. Vera, R. Y. Tsien, and R. Ting, "New dioxaborolane chemistry enables [18f]-positron-emitting, fluorescent [18f]-multimodality biomolecule generation from the solid phase," *Bioconjugate chemistry*, vol. 27, no. 5, pp. 1390–1399, 2016.

[8] P. Moskal, I. Moskal, and G. Moskal, "Tof-pet tomograph and a method of imaging using a tof-pet tomograph, based on a probability of production and lifetime of a positronium," Dec. 26 2017, uS Patent 9,851,456.

[9] D. J. Kadrmas, "Lor-osem: statistical pet reconstruction from raw line-of-response histograms," *Physics in Medicine & Biology*, vol. 49, no. 20, p. 4731, 2004.

[10] G. T. Herman, "Image reconstruction from projections," *Real-Time Imaging*, vol. 1, no. 1, pp. 3–18, 1995.

[11] L. A. Shepp and Y. Vardi, "Maximum likelihood reconstruction for emission tomography," *IEEE transactions on medical imaging*, vol. 1, no. 2, pp. 113–122, 1982.

[12] H. M. Hudson and R. S. Larkin, "Accelerated image reconstruction using ordered subsets of projection data," *IEEE transactions on medical imaging*, vol. 13, no. 4, pp. 601–609, 1994.

[13] S. Tong, A. M. Alessio, and P. E. Kinahan, "Image reconstruction for pet/ct scanners: past achievements and future challenges," *Imaging in medicine*, vol. 2, no. 5, p. 529, 2010.

[14] D. Swinehart, "The beer-lambert law," *Journal of chemical education*, vol. 39, no. 7, p. 333, 1962.

[15] C. L. Melcher, "Scintillation crystals for pet," *Journal of Nuclear Medicine*, vol. 41, no. 6, pp. 1051–1055, 2000.

[16] S.-J. Park, W. L. Rogers, and N. H. Clinthorne, "Improvement of noise equivalent count rate using compton kinematics in a compton pet," *IEEE Transactions on Nuclear Science*, vol. 54, no. 5, pp. 1589–1598, 2007.

[17] A. Nassalski, M. Kapusta, T. Batsch, D. Wolski, D. Mockel, W. Enghardt, and M. Moszynski, "Comparative study of scintillators for pet/ct detectors," in *Nuclear Science Symposium Conference Record, 2005 IEEE*, vol. 5. IEEE, 2005, pp. 2823–2829.

[18] V. C. Spanoudaki and C. S. Levin, "Photo-detectors for time of flight positron emission tomography (tof-pet)," *Sensors*, vol. 10, no. 11, pp. 10 484–10 505, 2010.

[19] Y. Gu, G. Pratx, F. W. Lau, and C. S. Levin, "Effects of multiple-interaction photon events in a high-resolution pet system that uses 3-d positioning detectors," *Medical physics*, vol. 37, no. 10, pp. 5494–5508, 2010.

[20] M. Conti, "State of the art and challenges of time-of-flight pet," *Physica Medica: European Journal of Medical Physics*, vol. 25, no. 1, pp. 1–11, 2009.

[21] Y. Gu, "High-resolution small animal positron emission tomography system based on 3-d position-sensitive cadmium zinc telluride photon detectors," Ph.D. dissertation, Stanford University, 2014.

[22] W. W. Moses, "Fundamental limits of spatial resolution in pet," *Nuclear Instruments and Methods in Physics Research Section A: Accelerators, Spectrometers, Detectors and Associated Equipment*, vol. 648, pp. S236–S240, 2011.

[23] C. S. Levin and E. J. Hoffman, "Calculation of positron range and its effect on the fundamental limit of positron emission tomography system spatial resolution," *Physics in Medicine & Biology*, vol. 44, no. 3, p. 781, 1999.

[24] S. R. Cherry, J. A. Sorenson, and M. E. Phelps, *Physics in nuclear medicine e-Book*. Elsevier Health Sciences, 2012.

[25] L. R. MacDonald and M. Dahlbom, "Parallax correction in pet using depth of interaction information," *IEEE Transactions on Nuclear Science*, vol. 45, no. 4, pp. 2232–2237, 1998.

[26] R. L. Siegel, K. D. Miller, and A. Jemal, "Cancer statistics, 2017," *CA: A Cancer Journal for Clinicians*, vol. 67, pp. 7–30, 2017.

[27] R. Subramaniam, M. Truong, P. Peller, O. Sakai, and G. Mercier, "Fluorodeoxyglucose–positron-emission tomography imaging of head and neck squamous cell cancer," *American Journal of Neuroradiology*, vol. 31, no. 4, pp. 598–604, 2010.

[28] B. Nowak, E. Di Martino, S. Jänicke, U. Cremerius, G. Adam, M. Zimny, P. Reinartz, U. Büll et al., "Diagnostic evaluation of malignant head and neck cancer by F-18-FDG PET compared to CT/MRI," *Nuklearmedizin Archive*, vol. 38, no. 8, pp. 312–318, 1999.

[29] S.-M. Eschmann, F. Paulsen, M. Reimold, H. Dittmann, S. Welz, G. Reischl, H.-J. Machulla, and R. Bares, "Prognostic impact of hypoxia imaging with 18F-misonidazole PET in non-small cell lung cancer and head and neck cancer before radiotherapy," *Journal of nuclear medicine*, vol. 46, no. 2, pp. 253–260, 2005.

[30] D. L. Schwartz, E. Ford, J. Rajendran, B. Yueh, M. D. Coltrera, J. Virgin, Y. Anzai, D. Haynor, B. Lewellyn, D. Mattes et al., "FDG-PET/CT imaging for preradiotherapy staging of head-and-neck squamous cell carcinoma," *International Journal of Radiation Oncology* Biology* Physics*, vol. 61, no. 1, pp. 129–136, 2005.

[31] E. J. Hoffman, S.-C. Huang, and M. E. Phelps, "Quantitation in positron emission computed tomography: 1. Effect of object size." *Journal of computer assisted tomography*, vol. 3, no. 3, pp. 299–308, 1979.

[32] Y. Yamazaki, M. Saitoh, K.-i. Notani, K. Tei, Y. Totsuka, S.-i. Takinami, K. Kanegae, M. Inubushi, N. Tamaki, and Y. Kitagawa, "Assessment of cervical lymph node metastases using FDG-PET in patients with head and neck cancer," *Annals of nuclear medicine*, vol. 22, no. 3, pp. 177–184, 2008.

[33] Y. Yamamoto, T. Z. Wong, T. G. Turkington, T. C. Hawk, and R. E. Coleman, "Head and neck cancer: dedicated FDG PET/CT protocol for detectionphantom and initial clinical stsudies," *Radiology*, vol. 244, no. 1, pp. 263–272, 2007.

[34] R. S. Rodrigues, F. A. Bozza, P. E. Christian, J. M. Hoffman, R. I. Butterfield, C. R. Christensen, M. Heilbrun, R. H. Wiggins, J. P. Hunt, B. G. Bentz et al., "Comparison of whole-body PET/CT, dedicated high-resolution head and neck PET/CT, and contrast-enhanced CT in preoperative staging of clinically M0 squamous cell carcinoma of the head and neck," *Journal of Nuclear Medicine*, vol. 50, no. 8, pp. 1205–1213, 2009.

[35] A. Argiris, M. V. Karamouzis, D. Raben, and R. L. Ferris, "Head and neck cancer," *The Lancet*, vol. 371, no. 9625, pp. 1695–1709, 2008.

[36] E. M. Rohren, T. G. Turkington, and R. E. Coleman, "Clinical applications of PET in oncology," *Radiology*, vol. 231, no. 2, pp. 305–332, 2004.

[37] A. Santos, P. Almeida, M. Martins, N. Matela, N. Oliveira, N. Ferreira, J. Aguiar, F. Almeida, F. Lopes, J. Sampaio et al., "Design and evaluation of the clear-pem detector for positron emission mammography," in *Nuclear Science Symposium Conference Record, 2004 IEEE*, vol. 6. IEEE, 2004, pp. 3805–3809.

[38] J. Zhang, P. D. Olcott, G. Chinn, A. M. Foudray, and C. S. Levin, "Study of the performance of a novel 1mm resolution dual-panel pet camera design dedicated to breast cancer imaging using monte carlo simulation," *Medical physics*, vol. 34, no. 2, pp. 689–702, 2007.

[39] H. Peng and C. S. Levin, "Design study of a high-resolution breast-dedicated pet system built from cadmium zinc telluride detectors," *Physics in Medicine & Biology*, vol. 55, no. 9, p. 2761, 2010.

[40] M. Wang, G. Hu, and H. Zhang, "Performance comparison of dual-head pem scanner by monte carlo simulation," *Nuclear Instruments and Methods in Physics Research Section A: Accelerators, Spectrometers, Detectors and Associated Equipment*, vol. 737, pp. 5–10, 2014.

[41] C. Zeng, P. E. Kinahan, H. Qian, R. L. Harrison, K. E. Champley, and L. R. MacDonald, "Simulation study of quantitative precision of the pet/x dedicated breast pet scanner," *Journal of Medical Imaging*, vol. 4, no. 4, p. 045502, 2017.

[42] K. Gong, S. Majewski, P. E. Kinahan, R. L. Harrison, B. F. Elston, R. Manjeshwar, S. Dolinsky, A. V. Stolin, J. A. Brefczynski-Lewis, and J. Qi, "Designing a compact high performance brain pet scannersimulation study," *Physics in Medicine & Biology*, vol. 61, no. 10, p. 3681, 2016.

[43] T. Yamaya, E. Yoshida, H. Tashima, N. Inadama, T. Shinaji, H. Wakizaka, M. Nitta, S. Tazawa, T. Suhara, and Y. Fujibayashi, "First prototype of a compact helmet-chin pet for high-sensitivity brain imaging," *Journal of Nuclear Medicine*, vol. 56, no. supplement 3, pp. 317–317, 2015.

[44] C. E. Bauer, J. Brefczynski-Lewis, G. Marano, M.-B. Mandich, A. Stolin, P. Martone, J. W. Lewis, G. Jaliparthi, R. R. Raylman, and S. Majewski, "Concept of an upright wearable positron emission tomography imager in humans," *Brain and behavior*, vol. 6, no. 9, 2016.

[45] C. R. Schmidtlein, J. N. Turner, M. O. Thompson, K. C. Mandal, I. Häggström, J. Zhang, J. L. Humm, D. H. Feiglin, and A. Krol, "Initial performance studies of a wearable brain positron emission tomography camera based on autonomous thin-film digital geiger avalanche photodiode arrays," *Journal of Medical Imaging*, vol. 4, no. 1, p. 011003, 2016.

[46] J. A. Kolthammer, K.-H. Su, A. Grover, M. Narayanan, D. W. Jordan, and R. F. Muzic, "Performance evaluation of the ingenuity tf pet/ct scanner with a focus on high count-rate conditions," *Physics in Medicine & Biology*, vol. 59, no. 14, p. 3843, 2014.

[47] B. Jakoby, Y. Bercier, M. Conti, M. Casey, B. Bendriem, and D. Townsend, "Physical and clinical performance of the mct time-of-flight pet/ct scanner," *Physics in Medicine & Biology*, vol. 56, no. 8, p. 2375, 2011.

[48] V. Bettinardi, L. Presotto, E. Rapisarda, M. Picchio, L. Gianolli, and M. Gilardi, "Physical performance of the new hybrid pet/ct discovery-690," *Medical physics*, vol. 38, no. 10, pp. 5394–5411, 2011.

[49] M. Miller, J. Zhang, K. Binzel, J. Griesmer, T. Laurence, M. Narayanan, D. Natarajamani, S. Wang, and M. Knopp, "Characterization of the vereos digital photon counting pet system," *Journal of Nuclear Medicine*, vol. 56, no. supplement 3, pp. 434–434, 2015.

[50] K. Burr, G.-C. Wang, H. Du, G. Mann, K. Balakrishnan, J. Wang, X. Li, C. Rollet, E. Kundro, M. Buhin et al., "A new modular and scalable detector for a time-of-flight pet scanner," in *Nuclear Science Symposium and Medical Imaging Conference (NSS/MIC), 2012 IEEE*. IEEE, 2012, pp. 2830–2834.

[51] T. Kimble, M. Chou, and B. H. Chai, "Scintillation properties of lyso crystals," in *Nuclear Science Symposium Conference Record, 2002 IEEE*, vol. 3. IEEE, 2002, pp. 1434–1437.

[52] J.-H. Lee, S. Hwang, C. L. Istook et al., "Analysis of human head shapes in the united states," *International Journal of Human Ecology*, vol. 7, no. 1, pp. 77–83, 2006.

[53] C. M. Pepin, P. Bérard, A.-L. Perrot, C. Pépin, D. Houde, R. Lecomte, C. L. Melcher, and H. Dautet, "Properties of LYSO and recent LSO scintillators for phoswich PET detectors," *IEEE Transactions on Nuclear Science*, vol. 51, no. 3, pp. 789–795, 2004.

[54] S. Jan, G. Santin, D. Strul, S. Staelens, K. Assie, D. Autret, S. Avner, R. Barbier, M. Bardies, P. Bloomfield et al., "GATE: a simulation toolkit for PET and SPECT," *Physics in medicine and biology*, vol. 49, no. 19, p. 4543, 2004.

[55] G. Sportelli, S. Ahmad, N. Belcari, M. G. Bisogni, N. Camarlinghi, A. Di Pasquale, S. Dussoni, J. Fleury, M. Morrocchi, E. Zaccaro et al., "The TRIMAGE PET Data Acquisition System: Initial Results," *IEEE Transactions on Radiation and Plasma Medical Sciences*, vol. 1, no. 2, pp. 168–177, 2017.

[56] S. Majewski, J. Proffitt, J. Brefczynski-Lewis, A. Stolin, A. Weisenberger, W. Xi, and R. Wojcik, "HelmetPET: A silicon photomultiplier based wearable brain imager," in *Nuclear Science Symposium and Medical Imaging Conference (NSS/MIC), 2011 IEEE*. IEEE, 2011, pp. 4030–4034.

[57] D. F. Hsu, E. Ilan, W. T. Peterson, J. Uribe, M. Lubberink, and C. S. Levin, "Studies of a Next Generation Silicon-Photomultiplier-Based Time-of-Flight PET/CT System," *Journal of Nuclear Medicine*, pp. jnumed–117, 2017.

[58] S. Strother, M. Casey, and E. Hoffman, "Measuring PET scanner sensitivity: relating countrates to image signal-to-noise ratios using noise equivalents counts," *IEEE Transactions on Nuclear Science*, vol. 37, no. 2, pp. 783–788, 1990.

[59] H. A. Sorenson, M. E. Phelps et al., *Physics in nuclear medicine*. Saunders Philadelphia, 1987.

[60] J. Cui, G. Pratx, B. Meng, and C. S. Levin, "Distributed MLEM: An iterative tomographic image reconstruction algorithm for distributed memory architectures," *IEEE transactions on medical imaging*, vol. 32, no. 5, pp. 957–967, 2013.

[61] S. Abbaszadeh, G. Chinn, and C. S. Levin, "Positioning true coincidences that undergo inter-and intra-crystal scatter for a sub-mm resolution cadmium zinc telluride-based PET system," *Physics in Medicine & Biology*, vol. 63, no. 2, p. 025012, 2018.

[62] J. E. Gillam, P. Solevi, J. F. Oliver, C. Casella, M. Heller, C. Joram, and M. Rafecas, "Sensitivity recovery for the AX-PET prototype using inter-crystal scattering events," *Physics in medicine and biology*, vol. 59, no. 15, p. 4065, 2014.

[63] A. A. Wagadarikar, A. Ivan, S. Dolinsky, and D. L. McDaniel, "Sensitivity improvement of time-of-flight (TOF)-PET detector through recovery of Compton scattered annihilation photons," in *Nuclear Science Symposium and Medical Imaging Conference (NSS/MIC), 2012 IEEE*. IEEE, 2012, pp. 3178–3183.

[64] E. Yoshida, H. Tashima, and T. Yamaya, "Sensitivity booster for DOI-PET scanner by utilizing Compton scattering events between detector blocks," *Nuclear Instruments and Methods in Physics Research Section A: Accelerators, Spectrometers, Detectors and Associated Equipment*, vol. 763, pp. 502–509, 2014.

[65] R. Freifelder and J. S. Karp, "Dedicated PET scanners for breast imaging," *Physics in Medicine and Biology*, vol. 42, no. 12, p. 2463, 1997.

[66] L. Fin, P. Bailly, J. Daouk, and M.-E. Meyer, "A practical way to improve contrast-to-noise ratio and quantitation for statistical-based iterative reconstruction in whole-body PET imaging," *Medical physics*, vol. 36, no. 7, pp. 3072–3079, 2009.

[67] A. M. Alessio, P. E. Kinahan, P. M. Cheng, H. Vesselle, and J. S. Karp, "PET/CT scanner instrumentation, challenges, and solutions," *Radiologic Clinics of North America*, vol. 42, no. 6, pp. 1017–1032, 2004.